# Assessing Carrier Mobility, Dopability, and Defect Tolerance in the Chalcogenide Perovskite $BaZrS_3$

Zhenkun Yuan,[1,†] Diana Dahliah,[2,3,†] Romain Claes,[2,4] Andrew Pike,[1] David P. Fenning,[5] Gian-Marco Rignanese,[2] and Geoffroy Hautier[1,*]

[1] *Thayer School of Engineering, Dartmouth College, Hanover, New Hampshire 03755, USA*

[2] *Institute of Condensed Matter and Nanosciences, Université Catholique de Louvain, Chemin Étoiles 8, bte L7.03.01, 1348 Louvain-la-Neuve, Belgium*

[3] *Department of Physics, An-Najah National University, Nablus, Palestine*

[4] *School of Chemistry, University of Birmingham, Edgbaston, Birmingham, B15 2TT, United Kingdom*

[5] *Department of Chemical and Nano Engineering, University of California, San Diego, La Jolla, California 92093, USA*

(Received 27 May 2024; revised 10 August 2024; accepted 3 September 2024; published 30 September 2024)

The chalcogenide perovskite $BaZrS_3$ has attracted much attention as a promising solar absorber for thin-film photovoltaics. Here we use first-principles calculations to evaluate its carrier transport and defect properties. We find that $BaZrS_3$ has a phonon-limited electron mobility of 37 $cm^2/V\,s$, which is comparable to that in halide perovskites, but lower hole mobility of 11 $cm^2/V\,s$. The defect computations indicate that $BaZrS_3$ is intrinsically *n*-type due to shallow sulfur vacancies, but that strong compensation by sulfur vacancies will prevent attempts to make it *p*-type. We also establish that $BaZrS_3$ shows some degree of defect tolerance, presenting only few low formation energy, deep intrinsic defects. Among the deep defects, sulfur interstitials are the dominant nonradiative recombination centers but exhibit a moderate capture coefficient. Our work highlights the material's intrinsic limitations in carrier mobility and *p*-type doping, and suggests focusing on suppressing the formation of sulfur interstitials to achieve longer carrier lifetime.

DOI: 10.1103/PRXEnergy.3.033008

## I. INTRODUCTION

Lead halide perovskites have revolutionized the field of photovoltaics (PVs) by opening a promising path to earth-abundant, easily processable, and high-efficiency thin-film technologies [1,2]. The exceptional PV performance of halide perovskites is, however, overshadowed by their poor stability [3–5]. Structural analogy has motivated the search for alternative solar absorbers forming in the perovskite structure but in chemistries that could be more stable [6–15]. The chalcogenide perovskites $ABX_3$ ($A$ = Ca, Sr, Ba; $B$ = Ti, Zr, Hf; and $X$ = S, Se) have emerged in this context, with their first suggestion as solar absorbers coming from first-principles studies [6], followed by experimental synthesis and characterization especially of $BaZrS_3$ [16–20]. $BaZrS_3$ shows excellent stability in ambient conditions and exhibits a direct band gap of approximately 1.8 eV that can be tuned to 1.5 eV by alloying with $BaTiS_3$ or $BaZrSe_3$ [16,18–26]. Significant efforts have been dedicated to growing high-quality thin films of $BaZrS_3$ and its alloys, by a range of techniques, such as pulsed laser deposition [27–30], sputtering [22,31,32], molecular beam epitaxy [33,34], and solution-based synthesis [35–37]. Very recently, a proof-of-concept $BaZrS_3$ solar cell was reported, demonstrating an efficiency of 0.11% [38]. Interestingly, $BaZrS_3$ also stands out as a top candidate in a few high-throughput computational screenings of thin-film solar absorbers [12,39–41].

In this work, we use first-principles calculations to clarify the carrier transport and defect properties in $BaZrS_3$. We compute the phonon-limited carrier mobility, showing that $BaZrS_3$ has intrinsically low hole mobility. We also perform state-of-the-art hybrid-functional defect calculations. We show that $BaZrS_3$ is intrinsically *n*-type, and that *p*-type doping of $BaZrS_3$ will be very difficult due to strong compensation by intrinsic donor defects. We identify the sulfur interstitial ($S_i$) as the main deep defect, but show that its nonradiative capture coefficient is moderate and that

*Contact author: geoffroy.hautier@dartmouth.edu

†These authors contributed equally to this work.

sulfur chemical potential control should mitigate its impact on the carrier lifetime in $BaZrS_3$. Our results suggest pathways regarding growth condition optimization and device design towards high-performance $BaZrS_3$ absorbers.

## II. RESULTS

### A. Electronic band structure and carrier transport

$BaZrS_3$ forms in an orthorhombic *Pnma* perovskite structure [Fig. 1(a)]. Our calculated electronic band structure obtained with use of the Heyd-Scuseria-Ernzerhof hybrid functional (HSE06) [42] shows a direct band gap of 1.81 eV at the Γ point [Fig. 1(b)], in agreement with previous calculations and experiments [6,12,18–24,43]. Combining computed electronic and phonon properties, we find a phonon-limited carrier mobility of 11 $cm^2/V\,s$ for holes and 37 $cm^2/V\,s$ for electrons at room temperature (see Sec. V A for details), with the carrier scattering mechanism dominated by polar optical phonons. These values are upper bounds as realistic polycrystalline films will have additional scatterings from, e.g., grain boundaries and impurities. They are much lower than those calculated for conventional thin-film inorganic solar absorbers (such as CdTe [44,45] and $Cu_2ZnSnS_4$ [46]). The calculated hole mobility of $BaZrS_3$ is also lower than for the halide perovskite $CH_3NH_3PbI_3$ (11 $cm^2/V\,s$ vs 47 $cm^2/V\,s$), yet these two materials have comparable calculated electron mobility [47]. Our results are consistent with results from experiments on $BaZrS_3$ thin films that indicate low carrier mobilities (approximately 2 $cm^2/V\,s$ for holes and approximately 10–20 $cm^2/V\,s$ for electrons) [27,28,35,48]. The measured low carrier mobility has been often attributed to small grain size or impurity scattering [27,28]. While these could be limiting factors in the experiments, our results highlight that $BaZrS_3$ has intrinsically low phonon-limited carrier mobility, and that experimentally it is very unlikely to achieve mobilities higher than our computed values. We note that Ye *et al.* [49] reported a very high sum mobility (greater than 100 $cm^2/V\,s$) in $BaZrS_3$ films on the basis of time-resolved photoluminescence measurements, but the data suffer from reported very large uncertainty.

The large difference between hole and electron mobilities directly comes from the electronic band structure. The lower conduction bands are much more dispersive than the upper valence bands [Fig. 1(b)]. As a result, the effective mass is found to be small for electrons ($0.3m_0$) and relatively large for holes ($0.9m_0$). The fundamental difference in hole effective mass and mobility between $BaZrS_3$ and $CH_3NH_3PbI_3$ comes from the different electronic character in the valence band. While the halide perovskite mixes anion and cation orbitals, leading to a delocalized valence band [50], the sulfide shows a more ionic behavior, with the valence band being mainly of anion character [Fig. 1(b)].

### B. Intrinsic point defects and doping

We have calculated all the intrinsic point defects in $BaZrS_3$, including the vacancies ($V_{Ba}$, $V_{Zr}$, $V_S$), interstitials ($Ba_i$, $Zr_i$, $S_i$), and antisites ($Ba_{Zr}$, $Zr_{Ba}$, $Ba_S$, $S_{Ba}$, $Zr_S$, $S_{Zr}$). Our first-principles defect calculations are all performed with the HSE06 hybrid functional and a large $3 \times 3 \times 2$ supercell (360 atoms) with appropriate charge correction and spin polarization, which is different from previous first-principles calculations [18,51]. We provide the details of our method in Sec. V B and a comparison with previous calculations in Supplemental Material [52]. We note that some of the defects (e.g., $S_i$) involve several configurations that are close in energy. In the following, we report only results for the lowest-energy configurations, while those for metastable configurations can be found in Fig. S2 in Supplemental Material [52].

Figure 2 shows the formation energies of the intrinsic defects in $BaZrS_3$ for both S-poor and S-rich conditions (see Fig. S1 in Supplemental Material [52] for details). The

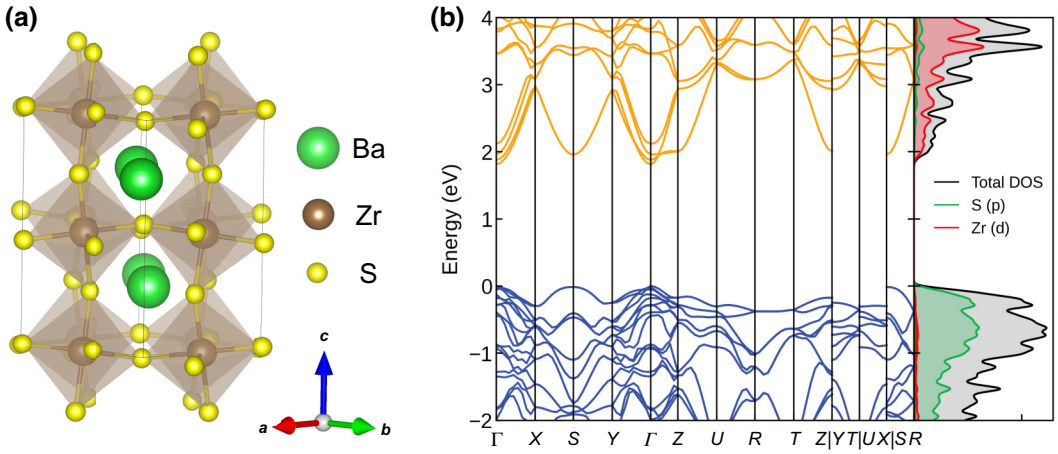


FIG. 1. (a) Crystal structure of $BaZrS_3$. (b) HSE06-calculated electronic band structure and (partial) density of states (DOS) of $BaZrS_3$.

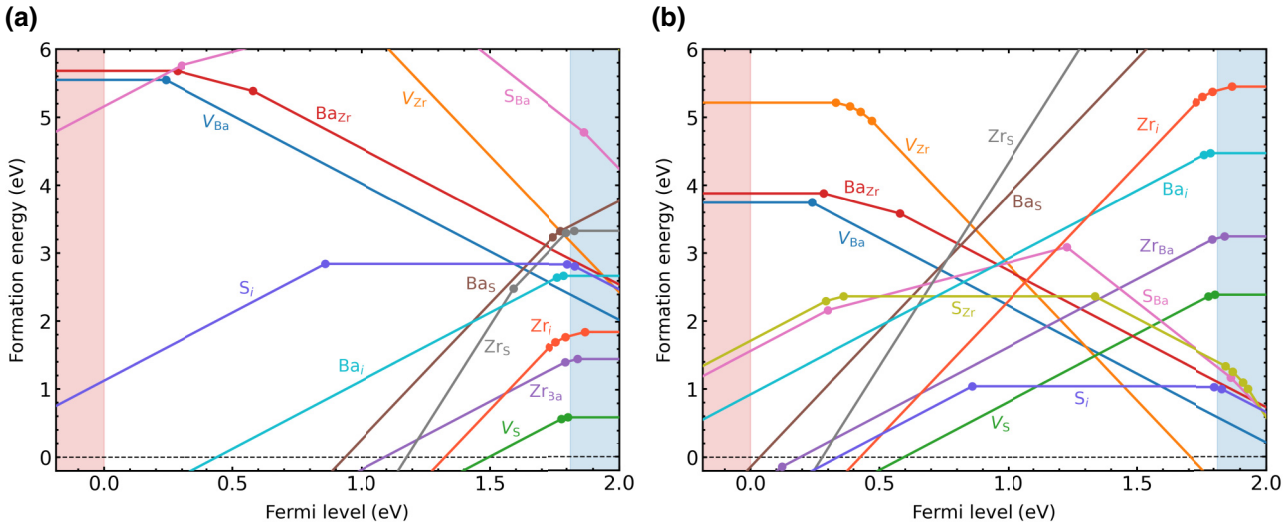


FIG. 2. Formation energies of intrinsic point defects in $BaZrS_3$ as a functional of the Fermi level, under (a) S-poor and (b) S-rich conditions. The Fermi level is referenced to the VBM of $BaZrS_3$. The slopes of the formation-energy lines indicate defect charge states, and the dots denote charge-state transition levels (see also Fig. 3).

defect charge-state transition levels are plotted in Fig. 3. We find that a series of shallow donor defects can form in $BaZrS_3$. $V_S$ is the dominant donor, giving rise to two donor levels (+/0) and (2+/+) that are almost in resonance with the conduction band. Under S-poor conditions [Fig. 2(a)], $V_S$ has fairly low formation energy and thus exists in high concentration. On the other hand, the acceptor defects, mainly $V_{Ba}$ and $Ba_{Zr}$, have high formation energies. These data indicate that S-poor $BaZrS_3$ will be heavily *n*-type doped by the $V_S$ donors. Under S-rich conditions [Fig. 2(b)], the formation energy of $V_S$ is increased, while the formation energies of the acceptor defects are reduced. Under those conditions, the equilibrium Fermi level would be pinned close to the intersection of the formation energies of $V_S$ and $V_{Zr}$ (about 0.5 eV below the conduction band), indicative of a very weak *n*-type, almost intrinsic $BaZrS_3$. Our results explain the experimental observation that as-grown $BaZrS_3$ is intrinsically *n*-type, with the electron concentration as high as $10^{19}$–$10^{20}$ $cm^{-3}$ [27], and we attribute this doping to sulfur vacancies. Very recently, Aggarwal *et al.* [53] showed that $BaZrS_3$ films synthesized in a S-rich atmosphere are insulating but become *n*-type conductive with subsequent annealing in a high vacuum (i.e., a S-poor environment). They attributed this transition to the formation of sulfur vacancies. Additionally, they found no significant change in conductivity with variation of Ba:Zr ratio. These findings agree with our calculations.

Figure 2 also indicates that it will be very difficult to achieve *p*-type $BaZrS_3$. While $V_{Ba}$, $V_{Zr}$, and $Ba_{Zr}$ are shallow acceptors, they are strongly compensated by the $V_S$ donors. Even under the most favorable S-rich conditions, the Fermi-level pinning energy for *p*-type doping is 0.6 eV above the valence-band maximum (VBM), caused by the $V_S$, whose formation energy drops first to zero when the Fermi level is approaching the VBM [Fig. 2(b)]. In view of the high *p*-type pinning limit, any extrinsic shallow acceptors will be strongly compensated, thus preventing *p*-type doping [54–56]. In the literature, *p*-type $BaZrS_3$ has been reported only once, with a hole concentration of approximately $10^{18}$ $cm^{-3}$ [31]. We note that this was achieved in a sample that is extremely Ba deficient (Ba:Zr ratio as low as approximately 0.6), raising questions about possible secondary phases [57].

Next to doping, from Figs. 2 and 3 we identify a few defects with deep transition levels, including $V_{Zr}$ (3−/4−), $Ba_{Zr}$ (−/2−), $S_{Ba}$ (+/3−), $S_{Zr}$ (0/2−), and $S_i$ (0/2+). Only $S_i$ has sufficiently low formation energy to exist in significant concentrations (when in S-rich conditions; see Table S4 in Supplemental Material [52] for the calculated defect concentrations). Since defect-assisted nonradiative recombination is one of the key processes that limit carrier lifetime and ultimately solar cell performance [58–64], it is necessary to assess whether $S_i$ is an efficient nonradiative carrier recombination center. We note that the charge-compensated Frenkel pair [$V_S + S_i$] might form in $BaZrS_3$, considering that $S_i$ can also occur in negative charge states (i.e., acceptor-like behavior). However, the binding energy of this defect pair is found to be relatively small (0.74 eV; see Sec. V B), suggesting that it will not be very stable in the high-temperature processing of $BaZrS_3$.

### C. Nonradiative carrier capture by sulfur interstitials

We now compute the nonradiative carrier capture coefficients of $S_i$ (see Sec. V C for computational details).

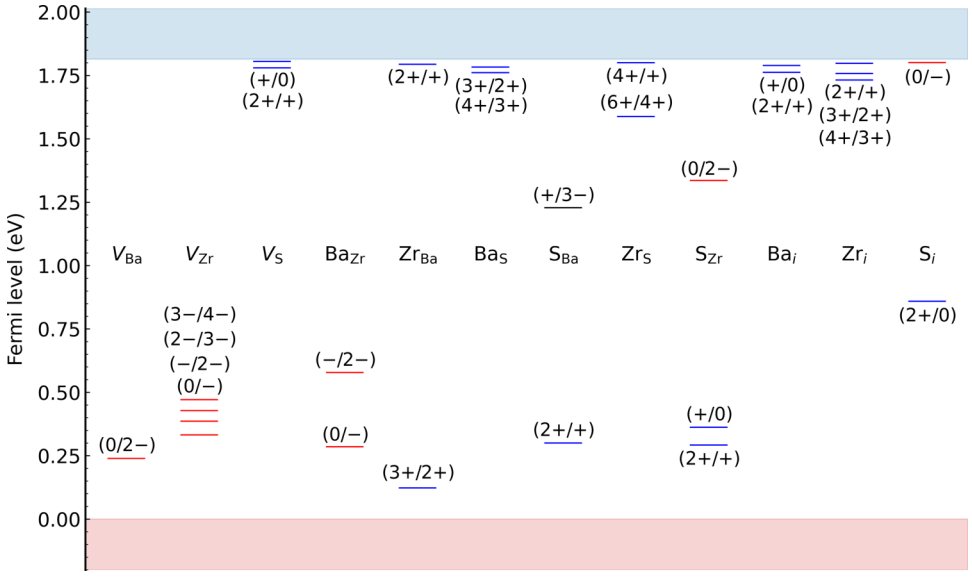


FIG. 3. Defect charge-state transition levels $\epsilon(q/q')$. Only the levels falling into the $BaZrS_3$ band gap are shown. The red and blue bars denote acceptor and donor levels, respectively.

For carrier capture by $S_i$, the relevant charge-state transitions are (+/0) and (2+/+), which are located at 0.35 and 1.37 eV above the VBM, respectively, as shown in Fig. 4(a). There are two capture processes for electron-hole recombination via the (+/0) level: $C_p^0$ for hole ($p$) capture and $C_n^+$ for electron ($n$) capture, where the superscript denotes the initial charge state. Similarly, recombination via the (2+/+) level involves two capture processes: $C_p^+$ and $C_n^{2+}$.

To illustrate the capture processes, Fig. 4(b) shows the local atomic structures of $S_i$ in the three charge states: 0, +, and 2+. The local structures of $S_i^0$ and $S_i^+$ are similar but differ from that of $S_i^{2+}$. In the 0 and + charge states, the interstitial S forms distorted tetrahedral bonds with two Ba nearest neighbors, one Zr nearest neighbor, and one S nearest neighbor. With the $S_i^0 \rightarrow S_i^+$ transition (i.e., capturing a hole, $C_p^0$), another lattice S atom moves towards the interstitial S. This lattice S atom and the interstitial S move further closer with the $S_i^+ \rightarrow S_i^{2+}$ transition (i.e., capturing another hole, $C_p^+$). As a result, $S_i^{2+}$ forms a S trimer.

The configuration coordinate diagrams for the $S_i^0 \rightleftharpoons S_i^+$ and $S_i^+ \rightleftharpoons S_i^{2+}$ transitions are shown in Figs. 4(c) and 4(d). Such diagrams map the potential energy surfaces of a defect in two adjacent charge states for a given transition as a function of a generalized configuration coordinate ($Q$) [65–67]. We find that the displacement $\Delta Q$ is larger between $S_i^+$ and $S_i^{2+}$ than between $S_i^0$ and $S_i^+$, reflecting the structural differences discussed above. The configuration coordinate diagrams indicate anharmonic atomic vibrations in the $S_i$ capture processes, specifically for the $S_i^+ \rightleftharpoons S_i^{2+}$ transitions, as shown in Fig. 4(d) (see also Fig. S3 in Supplemental Material [52]). Anharmonic potential energy surfaces have been widely found for nonradiative carrier capture in halide perovskites and other low-symmetry semiconductors [64,68–74]. As seen in Fig. 4(d), the anharmonicity substantially lowers the capture barriers as compared with the harmonic case; this leads to a vanishingly small hole capture barrier for $S_i^+$ and a moderate electron capture barrier of 0.27 eV for $S_i^{2+}$. In the case of $S_i^0 \rightleftharpoons S_i^+$ transitions, the hole capture barrier for $S_i^0$ is also nearly zero, and electron capture by $S_i^+$ has an energy barrier of 0.17 eV [Fig. 4(c)]. From the calculated capture barriers, we expect fast hole capture and slower electron capture by $S_i$.

Figure 4(e) shows the calculated capture coefficients of $S_i$ as a function of temperature. Consistent with the negligibly small hole capture barriers and the finite electron capture barriers, the capture coefficients indicate fast hole capture and much slower electron capture by $S_i$. Throughout the temperature range considered (200–500 K), the hole capture coefficient of $S_i^0$ ($C_p^0$) is as high as $10^{-6}$ cm$^3$/s, and that of $S_i^+$ ($C_p^+$) is on the order of $10^{-7}$ cm$^3$/s. In contrast, at 300 K, the electron capture coefficient of $S_i^+$ ($C_n^+$) is $1.54 \times 10^{-9}$ cm$^3$/s, and that of $S_i^{2+}$ ($C_n^{2+}$) has a moderate value of $7.18 \times 10^{-11}$ cm$^3$/s. For low-doped or intrinsic $BaZrS_3$, with balancing of electron and hole capture under steady-state conditions, the total capture coefficient ($C_{\text{tot}}$) of $S_i$ is given by [73,75]

$$C_{\text{tot}} = \frac{C_n^+ + C_p^+}{1 + \frac{C_n^+}{C_p^0} + \frac{C_p^+}{C_n^{2+}}}.$$

$C_{\text{tot}}$ of $S_i$ is calculated to be $7.27 \times 10^{-11}$ cm$^3$/s at 300 K [Fig. 4(e)]. $C_{\text{tot}}$ is limited by $C_n^{2+}$. The capture coefficient is moderate and is 2 orders of magnitude smaller than the

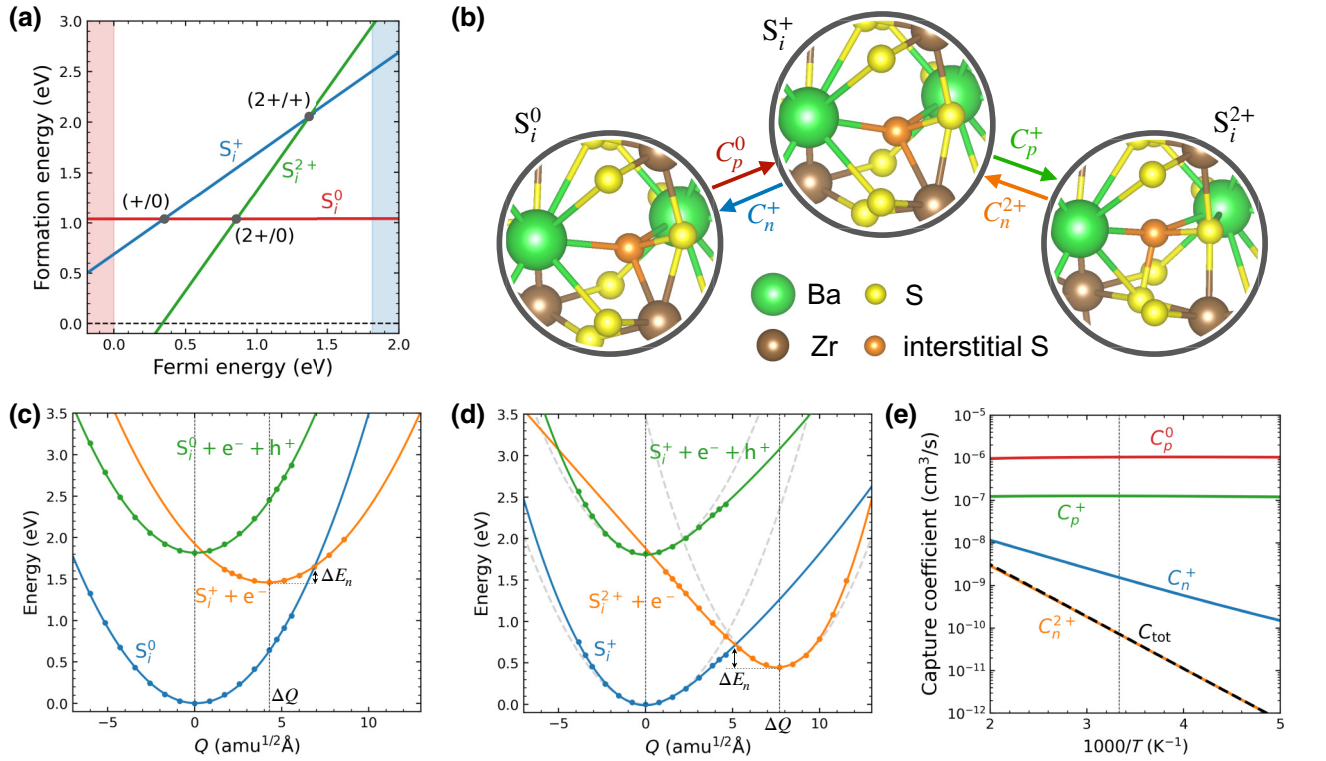


FIG. 4. (a) Formation energy of $S_i$ as a function of the Fermi level under S-rich conditions. (b) Local atomic structures of $S_i$ in the 0, +, and 2+ charge states. (c),(d) Configuration coordinate diagrams for the $S_i^0 \rightleftharpoons S_i^+$ and $S_i^+ \rightleftharpoons S_i^{2+}$ transitions. The data points represent potential energies obtained from first-principles calculations. In (c), the solid colored curves are parabolic fits to the data points and thus depict the potential energy surfaces in the harmonic approximation. In (d), the solid colored curves are potential energy surfaces obtained from quadratic spline fits to the data points, and the dashed gray curves are parabolic fits. $\Delta Q$ denotes the structural difference in configuration coordinate between the initial and final charge states, and $\Delta E_n$ denotes the electron capture barrier. (e) Temperature-dependent nonradiative capture coefficients of $S_i$.

value ($7 \times 10^{-9}$ cm$^3$/s) for the dominant recombination centers (iodine interstitials, $I_i$) in $CH_3NH_3PbI_3$ computed in a similar theoretical framework [68,70]. However, the capture coefficient of $S_i$ is not negligible. A high density of $S_i$ can still cause strong nonradiative recombination and limit the carrier lifetime.

## III. DISCUSSION

$BaZrS_3$ shows higher electron mobility than hole mobility, which would suggest the use of this material as a $p$-type absorber layer as it is the diffusion length of minority carriers that mainly controls the efficiency of $p$-$n$ junction solar cells [76–78]. Our analysis, however, shows that it will be unlikely to make a $p$-type $BaZrS_3$. Use of the intrinsically $n$-type doped $BaZrS_3$ as an absorber layer will lead to smaller minority-carrier diffusion lengths limited by the lower hole mobility and also cause issues at the device level as discussed for other $n$-type thin-film absorbers [79–81]. We thus suggest that it could be more viable to devise a $p$-$i$-$n$ (or $n$-$i$-$p$) cell with the use of $BaZrS_3$ as the intrinsic layer (lightly $n$-type doped), as in halide perovskite solar cells [82]. In such a $p$-$i$-$n$ device, the carrier diffusion length is controlled by the ambipolar mobility [83–85], which is estimated to be 17 cm$^2$/V s with our calculated intrinsic electron and hole mobilities. Preparation of intrinsic $BaZrS_3$ requires drastic reduction of the concentration of $V_S$ donors, which can be achieved under S-rich growth conditions [53]. However, S-rich conditions would enhance the formation of sulfur interstitials, which we have shown to be the main nonradiative recombination centers. It might be beneficial to reduce electron concentration by introducing an extrinsic shallow acceptor while keeping a low sulfur chemical potential.

Since high-quality $BaZrS_3$ films are typically deposited at a temperature of approximately 900 °C or higher [22,27,29,48], we estimate now a realistic upper bound of the $S_i$ density in high-temperature-synthesized $BaZrS_3$ samples. Under S-rich conditions [which corresponds to the defect formation energies displayed in Fig. 2(b)] and assuming 1000-K growth of $BaZrS_3$ and rapid quenching to room temperature, the $S_i$ density is estimated to be $4.14 \times 10^{17}$ cm$^{-3}$ (see Table S4). This high $S_i$ density leads to a nonradiative recombination coefficient ($A$) of $3.01 \times 10^7$ s$^{-1}$ at room temperature; here $A$ is defined as $A = N_d C_{tot}$, where $N_d$ is the defect density [70,86,87]. As

a result, the nonradiative lifetime ($\tau = 1/A$) is 33 ns for S-rich conditions. Under S-poor conditions and/or the use of a lower synthesis temperature will reduce the $S_i$ density and increase the carrier lifetime. We note though that growing $BaZrS_3$ at moderate temperatures tends to require S-rich conditions, as reported recently for synthesis of $BaZrS_3$ films at about 600 °C in the presence of excess sulfur [53,88,89]. Our results are in reasonable quantitative agreement with the carrier lifetime of about 50 ns measured by time-resolved photoluminescence experiments on $BaZrS_3$ single-crystal samples [49,90]. In comparison, $I_i$ in $CH_3NH_3PbI_3$ has been found to lead to a nonradiative lifetime on the order of 100 ns [68,70], on the basis of the deep-level trap density in solution-processed $CH_3NH_3PbI_3$ samples being on the order of $10^{15}$ $cm^{-3}$ [91–93].

Ye *et al.* [49] estimated the solar cell figure of merit ($F_{PV}$) of $BaZrS_3$ on the basis of experimental data and using $F_{PV} = \alpha L_D$, where $\alpha$ is the optical absorption coefficient and $L_D = \sqrt{\mu k_B T/e\tau}$ is the carrier diffusion length [83,94–96]. They found $F_{PV}$ to be 2.1 using an absorption coefficient of 4940 $cm^{-1}$, nonradiative lifetime of 50 ns, and ambipolar mobility of 146.2 $cm^2/V\,s$ [49]. Our computational results do not disagree with the carrier lifetime but raise strong doubts on the mobility value. Since our calculated ambipolar mobility is about an order of magnitude lower, we estimate $F_{PV}$ to be just 0.7. Our results, however, indicate that if the $S_i$ concentration is lowered or the interstitials are passivated in some way, higher carrier lifetime could be reached, which will increase the figure of merit.

In addition to intrinsic defects, we briefly mention that $BaZrS_3$ is tolerant to oxygen impurities, which could be present in high concentrations in the samples prepared by sulfurization of $BaZrO_3$ precursor [27,97]. We find that the oxygen-related point defects, including oxygen interstitial ($O_i$) and O substitution on the S site ($O_S$), are electrically inactive, i.e., they are stable in the neutral charge state for almost the entire range of Fermi levels (see Fig. S4 in Supplemental Material [52]), in agreement with the findings of previous experimental and theoretical studies [97].

## IV. CONCLUSIONS

We evaluated carrier transport and defect properties in the chalcogenide perovskite solar absorber $BaZrS_3$. Our results show that $BaZrS_3$ has a lower hole mobility than electron mobility (11 $cm^2/V\,s$ vs 37 $cm^2/V\,s$). The mobility in this sulfide perovskite is lower and more asymmetric (in terms of hole versus electron mobilities) than in lead halide perovskites. Our defect computations indicate an intrinsic tendency for *n*-type doping due to the shallow donor $V_S$ and that *p*-type doping is very unlikely to be achievable. $BaZrS_3$ shows favorable intrinsic defect behavior, with only few deep defects that could act as nonradiative recombination centers. Our computations further reveal that the most problematic deep defect, $S_i$, exhibits only a moderate nonradiative capture coefficient ($7.27 \times 10^{-11}$ $cm^3/s$). Under S-rich conditions, the carrier capture by $S_i$ will lead to a computed carrier lifetime of around 30 ns. $BaZrS_3$ exhibits some degree of defect tolerance, which is beneficial for its use as a solar absorber, and we suggest that suppressing the formation of $S_i$ will be critical in further increasing the carrier lifetime in $BaZrS_3$.

## V. METHODS

### A. Carrier mobility calculations

The phonon-limited carrier mobility was calculated with AMSET (*ab initio* scattering and transport). AMSET is a PYTHON package for performing efficient first-principles calculations of carrier scattering rates and transport in solid-state semiconductors and insulators [98]. It can account for different carrier scattering mechanisms, e.g., electron-phonon coupling. To prepare inputs for AMSET calculations, we calculated the material parameters of $BaZrS_3$ using the Vienna Ab initio Simulation Package (VASP) and the PBEsol functional [99–101]. A **k**-point grid of $8 \times 8 \times 6$ and an energy cutoff of 400 eV were found to converge the total energy of the *Pnma* unit cell structure of $BaZrS_3$ to within 1 meV/atom. In this work, only carrier scattering from polar optical phonons and acoustic deformation potentials was considered. For AMSET calculation of the carrier scattering rates, a dense **k**-point grid of $18 \times 18 \times 12$ was used to obtain the single-electron wave functions, which were used for calculation of the electron-phonon matrix elements from density-functional perturbation theory [102,103]. The calculated material parameters and full mobility tensor are detailed in Supplemental Material [52], with a discussion on possible errors.

### B. Defect calculations

The defect calculations were performed with VASP and the screened hybrid density functional of Heyd, Scuseria, and Ernzerhof (HSE06) [42,99,100]. The standard VASP projector augmented wave pseudopotentials (version PBE_54) were used: Ba_sv (ten valence electrons), Zr_sv (12 valence electrons), and S (six valence electrons). A plane-wave basis set with a cutoff of 400 eV was used to expand electron wave functions. Unless explicitly mentioned, these settings were used consistently in all our defect calculations.

The defect calculations started from relaxation of the $BaZrS_3$ orthorhombic *Pnma* unit cell. With a $6 \times 6 \times 4$ Γ-centered **k**-point mesh, the HSE06-calculated lattice constants are $a = 7.023$ Å, $b = 7.119$ Å, and $c = 10.006$ Å, in good agreement with previous HSE06 calculations and experimental findings [18,104]. On the basis of the HSE06-relaxed unit cell, a $3 \times 3 \times 2$ supercell that

contains 360 atoms was constructed and used for modeling point defects. For the supercell containing a point defect, all the internal atomic positions were fully relaxed with a force convergence criterion of 0.01 eV/Å. A Γ-only **k**-point mesh was used for the supercell calculations. Spin polarization was explicitly considered in all the defect calculations.

Defect formation energies were computed with the standard formalism [105,106]. As an example, the formation energy of sulfur vacancy ($V_S$) in charge state $q$, i.e., $V_S^q$, is given by

$$E_f(V_S^q) = E_{tot}(V_S^q) - E_{tot}(\text{bulk}) + \mu_S + qE_F + \Delta^q,$$

where $E_{tot}(V_S^q)$ and $E_{tot}(\text{bulk})$ are the total energies of the defect-containing and defect-free supercells, respectively. $\mu_S$ is the sulfur chemical potential, which can be understood as representing the sulfur content in the growth or annealing environment. Figure S1 in Supplemental Material [52] shows the chemical-potential stable region of $BaZrS_3$, which defines the allowed chemical-potential values for Ba, Zr, and S. Low $\mu_S$ values mean S-poor growth conditions, thus lowering the formation energy of sulfur vacancies, and vice versa. The electron Fermi level $E_F$ is referenced to the bulk VBM, and its position can be adjusted from the VBM to the conduction-band minimum (CBM). The term $\Delta^q$ is the finite-supercell-size correction for charged defects. We obtained charge corrections using the extended Freysoldt-Neugebauer–Van de Walle scheme [107,108] and the static dielectric constants ($\varepsilon_{xx} = 82.10$, $\varepsilon_{yy} = 70.67$, and $\varepsilon_{zz} = 85.46$, which include both electronic and ionic contributions calculated with the Perdew-Burke-Ernzerhof (PBE) functional [109]).

To correctly find the ground-state configuration of $S_i$, besides using the interstitial search algorithm implemented in the PyCDT code [110] to generate nine trial interstitial sites, we additionally generated another 13 trial interstitial sites purely on the basis of random numbers (although these random interstitial sites are required to have reasonable distances to the lattice sites).

Besides the isolated defects, the charge-compensated Frenkel pair [$V_S + S_i$] was also studied. Similarly to the search for the ground-state configuration of $S_i$, we generated 13 trial configurations for the [$V_S + S_i$] pair. The binding energy ($E_b$) of this defect pair was obtained as

$$E_b = E_f(V_S^{2+}) + E_f(S_i^{2-}) - E_f([V_S + S_i]).$$

A positive binding energy means energy gain for the formation of the defect pair, but entropy favors the isolated constituents [105,106,111].

In thermodynamic equilibrium, the concentration of a defect in the charge state $q$ (denoted as $D^q$) can be determined with use of its calculated formation energy:

$$C[D^q] = N_{sites} e^{-\frac{E_f(D^q)}{k_B T}},$$

where $N_{sites}$ is the number of sites (per unit volume) at which the defect can form, $k_B$ is the Boltzmann constant, and $T$ is the temperature. The equilibrium Fermi level can be determined by the charge-neutrality condition, which requires that the charges of positively charged defects and hole carriers balance the charges of negatively charged defects and electron carriers in the material [111–114]. This leads to a self-consistent solution of defect densities, carrier concentrations, and Fermi-level position. Often, materials are grown at high temperatures and measured at a lower temperature. To account for this, the defect densities can be computed at high temperatures, and one assumes that for each of the defect species, the total density is fixed to that at high temperatures but the charges are allowed to re-equilibrate so as to reach the charge-neutrality condition at a lower temperature. This is the so-called rapid quenching process [112–114].

Several PYTHON toolkits, including PyCDT [110], pymatgen [115], Pydefect [116], and py-sc-fermi [117], were used to generate initial defect structures, plot the chemical-potential phase diagram, and obtain defect formation energies and densities. We also mention here that the computer program VESTA [118] was used to visualize atomic geometries and the PYTHON toolkit sumo [119] was used to plot the electronic band structure.

### C. Nonradiative carrier capture calculations

The calculation of nonradiative carrier capture via multiphonon emission was based on a quantum mechanical 1D model [65–67,120,121]. In this 1D model, a generalized configuration coordinate ($Q$) is defined:

$$Q^2 = \sum_I M_I (\Delta \mathbf{R}_I)^2,$$

where $\Delta \mathbf{R}_I$ is the displacement of the $I$th atom of mass $M_I$ along the vector connecting the positions of this atom in the equilibrium defect structures of the initial and final charge states. As such, there is only one (effective) vibrational degree of freedom. For both charge states, obtaining a set of intermediate configurations by a linear interpolation or extrapolation between the two equilibrium structures and computation of their total energies lead to two potential energy surfaces. For each intermediate configuration, the electronic eigenstates were carefully checked to ensure that the defect states do not cross the band edges or undergo a change in occupation [64,71,122]. The two potential energy surfaces are offset horizontally (i.e., along the $Q$ axis) by $\Delta Q$, where $Q = \Delta Q$ and $Q = 0$ correspond to the equilibrium configurations of the initial and final

charge states, and offset vertically (i.e., along the energy axis) by $\Delta E$, where $\Delta E$ is the charge transition level referenced to the VBM (CBM) for hole (electron) capture. A third potential energy surface, which is the potential energy surface of the final charge state but shifted vertically by the band-gap value, is also needed to represent a free hole at the valence-band edge and a free electron at the conduction-band edge. With these, a configuration coordinate diagram is constructed for a carrier capture cycle (i.e., a complete process of nonradiative electron-hole recombination) [65,121]. From the configuration coordinate diagram, one can analyze the electron and hole capture barriers, which provide a qualitative estimate of how fast the capture processes are.

The carrier capture coefficients were computed on the basis of Fermi's golden rule in the static coupling theory [67,123]:

$$C(T) = gV\frac{2\pi}{\hbar}\sum_m w_m \sum_n |\langle \chi_{im}| Q - Q_0 |\chi_{fn}\rangle|^2 \times |W|^2 \delta(E_{im} - E_{fn}),$$

which requires computation of the overlap of vibrational wave functions and the electron-phonon coupling strength. In this equation, $\chi_{im}$ ($\chi_{fn}$) are vibrational wave functions of the potential energy surface for the initial (final) charge state, and are specified by a set of occupation numbers $\{m\}$ ($\{n\}$). $w_m$ is the thermal weight. $W = \langle \psi_b | \partial h/\partial Q | \psi_d \rangle$ is the electron-phonon matrix element in the first-order perturbation theory, where $\psi_b$ and $\psi_d$ are bulk and defect states for the single-particle electronic Hamiltonian $h$. The electron-phonon matrix element is evaluated at $Q_0$; $Q_0$ is a selected configuration that has a well-localized defect state in the band gap [67]. $g$ is the degeneracy factor of the final charge state. The $\delta$ function ensures energy conservation, where $E_{im}$ and $E_{fn}$ are total energies; in the harmonic approximation, $E_{im} - E_{fn} = \Delta E + m\hbar\omega_i - n\hbar\omega_f$, where $\omega_i$ and $\omega_f$ are phonon frequencies. We calculated the $W$ elements within the projector augmented wave formalism using VASP [124]. For carrier capture by a charged defect, $|W|$ was scaled by a Sommerfeld parameter ($s$), which accounts for the Coulomb attraction (or repulsion) between the delocalized carrier and charged defect. An additional scaling factor ($f$) was included for correction of the charge density near the defect when the $W$ elements are computed with a charged defect supercell. These scaling factors were computed with NONRAD [124]. The overlap of vibrational wave functions and final capture coefficients were determined with the CarrierCapture.jl code [122,125]. We performed carrier capture calculations for the deep defect $S_i$, with the key material parameters detailed in Table S5 in Supplemental Material [52].

## ACKNOWLEDGMENTS

This work was supported by the U.S. Department of Energy, Office of Science, Basic Energy Sciences under Award No. DE-SC0023509. This research used resources of the National Energy Research Scientific Computing Center (NERSC), a U.S. Department of Energy Office of Science User Facility, operated under Contract No. DE-AC02-05CH11231 using NERSC Award No. BES-ERCAP0023830. A.P. acknowledges support from a U.S. Department of Education Graduate Assistance in Areas of National Need fellowship.

## DATA AVAILABILITY

Input and output files for first-principles defect calculations in this work with relaxed defect structures are openly available on the NOMAD Repository [126], where files for the chemical-potential phase diagram, density of states, and (static) dielectric constant calculations are also available. Other data are available on reasonable request from the authors.

[1] A. Kojima, K. Teshima, Y. Shirai, and T. Miyasaka, Organometal halide perovskites as visible-light sensitizers for photovoltaic cells, J. Am. Chem. Soc. **131**, 6050 (2009).
[2] U.S. National Renewable Energy Laboratory, Best Research-Cell Efficiency Chart, https://www.nrel.gov/pv/cell-efficiency.html.
[3] J.-P. Correa-Baena, M. Saliba, T. Buonassisi, M. Grätzel, A. Abate, W. Tress, and A. Hagfeldt, Promises and challenges of perovskite solar cells, Science **358**, 739 (2017).
[4] B.-w. Park and S. I. Seok, Intrinsic instability of inorganic–organic hybrid halide perovskite materials, Adv. Mater. **31**, 1805337 (2019).
[5] B. Li, S. Li, J. Gong, X. Wu, Z. Li, D. Gao, D. Zhao, C. Zhang, Y. Wang, and Z. Zhu, Fundamental understanding of stability for halide perovskite photovoltaics: The importance of interfaces, Chem **10**, 35 (2024).
[6] Y.-Y. Sun, M. L. Agiorgousis, P. Zhang, and S. Zhang, Chalcogenide perovskites for photovoltaics, Nano Lett. **15**, 581 (2015).
[7] S. Körbel, M. A. Marques, and S. Botti, Stability and electronic properties of new inorganic perovskites from high-throughput *ab initio* calculations, J. Mater. Chem. C **4**, 3157 (2016).
[8] X.-G. Zhao, J.-H. Yang, Y. Fu, D. Yang, Q. Xu, L. Yu, S.-H. Wei, and L. Zhang, Design of lead-free inorganic halide perovskites for solar cells via cation-transmutation, J. Am. Chem. Soc. **139**, 2630 (2017).
[9] K. Kuhar, A. Crovetto, M. Pandey, K. S. Thygesen, B. Seger, P. C. Vesborg, O. Hansen, I. Chorkendorff, and K. W. Jacobsen, Sulfide perovskites for solar energy conversion applications: computational screening and synthesis of the selected compound $LaYS_3$, Energy Environ. Sci. **10**, 2579 (2017).

[10] S. Chakraborty, W. Xie, N. Mathews, M. Sherburne, R. Ahuja, M. Asta, and S. G. Mhaisalkar, Rational design: A high-throughput computational screening and experimental validation methodology for lead-free and emergent hybrid perovskites, ACS Energy Lett. **2**, 837 (2017).

[11] S. Lu, Q. Zhou, Y. Ouyang, Y. Guo, Q. Li, and J. Wang, Accelerated discovery of stable lead-free hybrid organic-inorganic perovskites via machine learning, Nat. Commun. **9**, 3405 (2018).

[12] Z. Huo, S.-H. Wei, and W.-J. Yin, High-throughput screening of chalcogenide single perovskites by first-principles calculations for photovoltaics, J. Phys. D: Appl. Phys. **51**, 474003 (2018).

[13] Y. Cai, W. Xie, Y. T. Teng, P. C. Harikesh, B. Ghosh, P. Huck, K. A. Persson, N. Mathews, S. G. Mhaisalkar, M. Sherburne, *et al.*, High-throughput computational study of halide double perovskite inorganic compounds, Chem. Mater. **31**, 5392 (2019).

[14] J. Gebhardt, A. Gassmann, W. Wei, A. Weidenkaff, and C. Elsässer, Screening for sustainable and lead-free perovskite halide absorbers – A database collecting insight from electronic-structure calculations, Mater. Des. **234**, 112324 (2023).

[15] R. Wu and A. M. Ganose, Tilt-induced charge localisation in phosphide antiperovskite photovoltaics, J. Phys. Condens. Matter **7**, 015009 (2023).

[16] K. V. Sopiha, C. Comparotto, J. A. Márquez, and J. J. Scragg, Chalcogenide perovskites: Tantalizing prospects, challenging materials, Adv. Opt. Mater. **10**, 2101704 (2022).

[17] J. W. Choi, B. Shin, P. Gorai, R. L. Z. Hoye, and R. Palgrave, Emerging earth-abundant solar absorbers, ACS Energy Lett. **7**, 1553 (2022).

[18] W. Meng, B. Saparov, F. Hong, J. Wang, D. B. Mitzi, and Y. Yan, Alloying and defect control within chalcogenide perovskites for optimized photovoltaic application, Chem. Mater. **28**, 821 (2016).

[19] S. Perera, H. Hui, C. Zhao, H. Xue, F. Sun, C. Deng, N. Gross, C. Milleville, X. Xu, D. F. Watson, *et al.*, Chalcogenide perovskites – An emerging class of ionic semiconductors, Nano Energy **22**, 129 (2016).

[20] S. Niu, H. Huyan, Y. Liu, M. Yeung, K. Ye, L. Blankemeier, T. Orvis, D. Sarkar, D. J. Singh, R. Kapadia, *et al.*, Bandgap control via structural and chemical tuning of transition metal perovskite chalcogenides, Adv. Mater. **29**, 1604733 (2017).

[21] X. Wei, H. Hui, S. Perera, A. Sheng, D. F. Watson, Y.-Y. Sun, Q. Jia, S. Zhang, and H. Zeng, Ti-alloying of $BaZrS_3$ chalcogenide perovskite for photovoltaics, ACS Omega **5**, 18579 (2020).

[22] C. Comparotto, A. Davydova, T. Ericson, L. Riekehr, M. V. Moro, T. Kubart, and J. Scragg, Chalcogenide perovskite $BaZrS_3$: Thin film growth by sputtering and rapid thermal processing, ACS Appl. Energy Mater. **3**, 2762 (2020).

[23] I. Sadeghi, J. Van Sambeek, T. Simonian, M. Xu, K. Ye, T. Cai, V. Nicolosi, J. M. LeBeau, and R. Jaramillo, Expanding the perovskite periodic table to include chalcogenide alloys with tunable band gap spanning 1.5–1.9 eV, Adv. Funct. Mater. **33**, 2304575 (2023).

[24] K. Ye, I. Sadeghi, M. Xu, J. Van Sambeek, T. Cai, J. Dong, R. Kothari, J. M. LeBeau, and R. Jaramillo, A processing route to chalcogenide perovskites alloys with tunable band gap via anion exchange, Adv. Funct. Mater. 2405135 (2024).

[25] P. Kayastha, G. Longo, and L. D. Whalley, A first-principles thermodynamic model for the Ba–Zr–S system in equilibrium with sulfur vapor, ACS Appl. Energy Mater. (2024).

[26] R. Bystrickyy, S. K. Tiwari, P. Hutar, and M. Sykora, Thermal stability of chalcogenide perovskites, Inorg. Chem. **63**, 12826 (2024).

[27] X. Wei, H. Hui, C. Zhao, C. Deng, M. Han, Z. Yu, A. Sheng, P. Roy, A. Chen, J. Lin, *et al.*, Realization of $BaZrS_3$ chalcogenide perovskite thin films for optoelectronics, Nano Energy **68**, 104317 (2020).

[28] Z. Yu, X. Wei, Y. Zheng, H. Hui, M. Bian, S. Dhole, J.-H. Seo, Y.-Y. Sun, Q. Jia, S. Zhang, S. Yang, and H. Zeng, Chalcogenide perovskite $BaZrS_3$ thin-film electronic and optoelectronic devices by low temperature processing, Nano Energy **85**, 105959 (2021).

[29] S. P. Ramanandan, A. Giunto, E. Z. Stutz, B. Reynier, I. T. F. M. Lefevre, M. Rusu, S. Schorr, T. Unold, A. F. I. Morral, J. A. Márquez, *et al.*, Understanding the growth mechanism of $BaZrS_3$ chalcogenide perovskite thin films from sulfurized oxide precursors, J. Phys.: Energy **5**, 014013 (2023).

[30] M. Surendran, S. Singh, H. Chen, C. Wu, A. Avishai, Y.-T. Shao, and J. Ravichandran, A hybrid pulsed laser deposition approach to grow thin films of chalcogenides, Adv. Mater. **36**, 2312620 (2024).

[31] Y. Han, J. Xu, Y. Liang, X. Chen, M. Jia, J. Zhang, L. Lian, Y. Liu, X. Li, and Z. Shi, p-type conductive $BaZrS_3$ thin film and its band gap tunning via Ruddlesden-Popper $Ba_3Zr_2S_7$ and titanium alloying, Chem. Eng. J. **473**, 145351 (2023).

[32] S. Jamshaid, M. R. Cicconi, W. Heiss, K. G. Webber, and P. J. Wellmann, Synthesis and characterization of $BaZrS_3$ thin films via stacked layer methodology: A comparative study of $BaZrS_3$ on zirconium foil and silicon carbide substrates, Adv. Eng. Mater. **26**, 2302161 (2024).

[33] I. Sadeghi, K. Ye, M. Xu, Y. Li, J. M. LeBeau, and R. Jaramillo, Making $BaZrS_3$ chalcogenide perovskite thin films by molecular beam epitaxy, Adv. Funct. Mater. **31**, 2105563 (2021).

[34] M. Surendran, H. Chen, B. Zhao, A. S. Thind, S. Singh, T. Orvis, H. Zhao, J.-K. Han, H. Htoon, M. Kawasaki, *et al.*, Epitaxial thin films of a chalcogenide perovskite, Chem. Mater. **33**, 7457 (2021).

[35] V. K. Ravi, S. H. Yu, P. K. Rajput, C. Nayak, D. Bhattacharyya, D. S. Chung, and A. Nag, Colloidal $BaZrS_3$ chalcogenide perovskite nanocrystals for thin film device fabrication, Nanoscale **13**, 1616 (2021).

[36] J. W. Turnley, K. C. Vincent, A. A. Pradhan, I. Panicker, R. Swope, M. C. Uible, S. C. Bart, and R. Agrawal, Solution deposition for chalcogenide perovskites: a low-temperature route to $BaMS_3$ materials (M = Ti, Zr, Hf), J. Am. Chem. Soc. **144**, 18234 (2022).

[37] A. A. Pradhan, M. C. Uible, S. Agarwal, J. W. Turnley, S. Khandelwal, J. M. Peterson, D. D. Blach, R. N. Swope,

L. Huang, S. C. Bart, *et al.*, Synthesis of $BaZrS_3$ and $BaHfS_3$ chalcogenide perovskite films using single-phase molecular precursors at moderate temperatures, Angew. Chem. Int. Ed. **62**, e202301049 (2023).

[38] P. Dallas, K. Gkini, A. Kaltzoglou, L. Givalou, M. Konstantakou, S. Orfanoudakis, N. Boukos, E. Sakellis, P. Tsipas, A. Kalafatis, *et al.*, Exploring the potential of powder-to-film processing for proof-of-concept $BaZrS_3$ perovskite solar cells, Mater. Today Commun. **39**, 108608 (2024).

[39] Z. Yuan, D. Dahliah, M. R. Hasan, G. Kassa, A. Pike, S. Quadir, R. Claes, C. Chandler, Y. Xiong, V. Kyveryga, *et al.*, Discovery of the Zintl-phosphide $BaCd_2P_2$ as a long carrier lifetime and stable solar absorber, Joule **8**, 1412 (2024).

[40] K. Kuhar, M. Pandey, K. S. Thygesen, and K. W. Jacobsen, High-throughput computational assessment of previously synthesized semiconductors for photovoltaic and photoelectrochemical devices, ACS Energy Lett. **3**, 436 (2018).

[41] D. H. Fabini, M. Koerner, and R. Seshadri, Candidate inorganic photovoltaic materials from electronic structure-based optical absorption and charge transport proxies, Chem. Mater. **31**, 1561 (2019).

[42] J. Heyd, G. E. Scuseria, and M. Ernzerhof, Hybrid functionals based on a screened coulomb potential, J. Chem. Phys. **118**, 8207 (2003).

[43] J. M. Polfus, T. Norby, and R. Bredesen, Protons in oxysulfides, oxysulfates, and sulfides: a first-principles study of $La_2O_2S$, $La_2O_2SO_4$, $SrZrS_3$, and $BaZrS_3$, J. Phys. Chem. C **119**, 23875 (2015).

[44] A. M. Ganose, J. Park, A. Faghaninia, R. Woods-Robinson, K. A. Persson, and A. Jain, Efficient calculation of carrier scattering rates from first principles, Nat. Commun. **12**, 2222 (2021).

[45] N. Vukmirović, Calculations of electron mobility in II-VI semiconductors, Phys. Rev. B **104**, 085203 (2021).

[46] B. Monserrat, J.-S. Park, S. Kim, and A. Walsh, Role of electron-phonon coupling and thermal expansion on band gaps, carrier mobility, and interfacial offsets in kesterite thin-film solar cells, Appl. Phys. Lett. **112**, 193903 (2018).

[47] S. Poncé, M. Schlipf, and F. Giustino, Origin of low carrier mobilities in halide perovskites, ACS Energy Lett. **4**, 456 (2019).

[48] J. A. Márquez, M. Rusu, H. Hempel, I. Y. Ahmet, M. Kölbach, I. Simsek, L. Choubrac, G. Gurieva, R. Gunder, S. Schorr, and T. Unold, $BaZrS_3$ chalcogenide perovskite thin films by $H_2S$ sulfurization of oxide precursors, J. Phys. Chem. Lett. **12**, 2148 (2021).

[49] K. Ye, B. Zhao, B. T. Diroll, J. Ravichandran, and R. Jaramillo, Time-resolved photoluminescence studies of perovskite chalcogenides, Faraday Discuss. **239**, 146 (2022).

[50] W.-J. Yin, J.-H. Yang, J. Kang, Y. Yan, and S.-H. Wei, Halide perovskite materials for solar cells: A theoretical review, J. Mater. Chem. A **3**, 8926 (2015).

[51] X. Wu, W. Gao, J. Chai, C. Ming, M. Chen, H. Zeng, P. Zhang, S. Zhang, and Y.-Y. Sun, Defect tolerance in chalcogenide perovskite photovoltaic material $BaZrS_3$, Sci. China Mater. **64**, 2976 (2021).

[52] See Supplemental Material at http://link.aps.org/supplemental/10.1103/PRXEnergy.3.033008 for more computational details and additional data and discussions. It includes Tables S1–S5, Figs. S1–S4, and Refs. [9,18,32,44,51,101–103,106,127–133].

[53] G. Aggarwal, A. S. Mirza, S. Riva, C. Comparotto, R. J. Frost, S. Mukherjee, M. Morales-Masis, H. Rensmo, and J. S. Scragg, Charge transport and defects in sulfur-deficient chalcogenide perovskite $BaZrS_3$, arXiv:2405.17327.

[54] J. Robertson and S. Clark, Limits to doping in oxides, Phys. Rev. B **83**, 075205 (2011).

[55] A. Walsh and A. Zunger, Instilling defect tolerance in new compounds, Nat. Mater. **16**, 964 (2017).

[56] Z. Yuan and G. Hautier, First-principles study of defects and doping limits in CaO, Appl. Phys. Lett. **124**, 232101 (2024).

[57] K. C. Vincent, S. Agarwal, Z. Fan, A. S. M. Canizales, and R. Agrawal, Expanding the horizons for viable precursors and liquid fluxes for the synthesis of $BaZrS_3$ and related compounds, J. Mater. Chem. C **12**, 12521 (2024).

[58] I. Repins, H. Moutinho, S. Choi, A. Kanevce, D. Kuciauskas, P. Dippo, C. Beall, J. Carapella, C. DeHart, B. Huang, *et al.*, Indications of short minority-carrier lifetime in kesterite solar cells, J. Appl. Phys. **114**, 084507 (2013).

[59] R. E. Brandt, V. Stevanović, D. S. Ginley, and T. Buonassisi, Identifying defect-tolerant semiconductors with high minority-carrier lifetimes: Beyond hybrid lead halide perovskites, MRS Commun. **5**, 265 (2015).

[60] R. Jaramillo, M.-J. Sher, B. K. Ofori-Okai, V. Steinmann, C. Yang, K. Hartman, K. A. Nelson, A. M. Lindenberg, R. G. Gordon, and T. Buonassisi, Transient terahertz photoconductivity measurements of minority-carrier lifetime in tin sulfide thin films: Advanced metrology for an early stage photovoltaic material, J. Appl. Phys. **119**, 035101 (2016).

[61] J. S. Park, S. Kim, Z. Xie, and A. Walsh, Point defect engineering in thin-film solar cells, Nat. Rev. Mater. **3**, 194 (2018).

[62] J.-F. Guillemoles, T. Kirchartz, D. Cahen, and U. Rau, Guide for the perplexed to the Shockley–Queisser model for solar cells, Nat. Photonics **13**, 501 (2019).

[63] S. Kim, J. A. Márquez, T. Unold, and A. Walsh, Upper limit to the photovoltaic efficiency of imperfect crystals from first principles, Energy Environ. Sci. **13**, 1481 (2020).

[64] X. Wang, S. R. Kavanagh, D. O. Scanlon, and A. Walsh, Upper efficiency limit of $Sb_2Se_3$ solar cells, Joule **8**, 2105 (2024).

[65] D. Lang and C. Henry, Nonradiative recombination at deep levels in GaAs and GaP by lattice-relaxation multiphonon emission, Phys. Rev. Lett. **35**, 1525 (1975).

[66] K. Huang, Lattice relaxation and multiphonon transitions, Contemp. Phys. **22**, 599 (1981).

[67] A. Alkauskas, Q. Yan, and C. G. Van de Walle, First-principles theory of nonradiative carrier capture via multiphonon emission, Phys. Rev. B **90**, 075202 (2014).

[68] X. Zhang, M. E. Turiansky, J.-X. Shen, and C. G. Van de Walle, Iodine interstitials as a cause of nonradiative

recombination in hybrid perovskites, Phys. Rev. B **101**, 140101 (2020).
[69] L. D. Whalley, P. Van Gerwen, J. M. Frost, S. Kim, S. N. Hood, and A. Walsh, Giant Huang–Rhys factor for electron capture by the iodine intersitial in perovskite solar cells, J. Am. Chem. Soc. **143**, 9123 (2021).
[70] X. Zhang, M. E. Turiansky, J.-X. Shen, and C. G. Van de Walle, Defect tolerance in halide perovskites: A first-principles perspective, J. Appl. Phys. **131**, 090901 (2022).
[71] L. D. Whalley, Steric engineering of point defects in lead halide perovskites, J. Phys. Chem. C **127**, 15738 (2023).
[72] Y. Kumagai, S. R. Kavanagh, I. Suzuki, T. Omata, A. Walsh, D. O. Scanlon, and H. Morito, Alkali monopnictides: A new class of photovoltaic materials by element mutation, PRX Energy **2**, 043002 (2023).
[73] M. Huang, S. Wang, and S. Chen, Metastability and anharmonicity enhance defect-assisted nonradiative recombination in low-symmetry semiconductors, arXiv:2312.01733.
[74] J. Zhang, X. Zhang, M. E. Turiansky, and C. G. Van de Walle, Iodine vacancies do not cause nonradiative recombination in halide perovskites, PRX Energy **2**, 013008 (2023).
[75] A. Alkauskas, C. E. Dreyer, J. L. Lyons, and C. G. Van de Walle, Role of excited states in Shockley-Read-Hall recombination in wide-band-gap semiconductors, Phys. Rev. B **93**, 201304 (2016).
[76] A. Kitai, *Principles of Solar Cells, LEDs and Related Devices: The Role of the PN Junction* (John Wiley & Sons, Chichester, UK, 2018).
[77] T. Gokmen, O. Gunawan, and D. B. Mitzi, Minority carrier diffusion length extraction in $Cu_2ZnSn(Se, S)_4$ solar cells, J. Appl. Phys. **114**, 114511 (2013).
[78] M. A. Scarpulla, B. McCandless, A. B. Phillips, Y. Yan, M. J. Heben, C. Wolden, G. Xiong, W. K. Metzger, D. Mao, D. Krasikov, *et al.*, CdTe-based thin film photovoltaics: Recent advances, current challenges and future prospects, Sol. Energy Mater. Sol. Cells **255**, 112289 (2023).
[79] T. Hill, S. Grover, and J. Sites, in *2023 IEEE 50th Photovoltaic Specialists Conference (PVSC)*, (IEEE, San Juan, 2023), Vol. 1.
[80] K. Javaid, J. Yu, W. Wu, J. Wang, H. Zhang, J. Gao, F. Zhuge, L. Liang, and H. Cao, Thin film solar cell based on $ZnSnN_2$/SnO heterojunction, Phys. Status Solidi – Rapid Res. Lett. **12**, 1700332 (2018).
[81] T. Gershon, K. Sardashti, O. Gunawan, R. Mankad, S. Singh, Y. S. Lee, J. A. Ott, A. Kummel, and R. Haight, Photovoltaic device with over 5% efficiency based on an n-type $Ag_2ZnSnSe_4$ absorber, Adv. Energy Mater. **6**, 1601182 (2016).
[82] J.-Y. Shao, D. Li, J. Shi, C. Ma, Y. Wang, X. Liu, X. Jiang, M. Hao, L. Zhang, C. Liu, *et al.*, Recent progress in perovskite solar cells: Material science, Sci. China Chem. **66**, 10 (2023).
[83] S. Akel, A. Kulkarni, U. Rau, and T. Kirchartz, Relevance of long diffusion lengths for efficient halide perovskite solar cells, PRX Energy **2**, 013004 (2023).
[84] M. Wang, K. Wang, Y. Gao, J. I. Khan, W. Yang, S. De Wolf, and F. Laquai, Impact of photoluminescence reabsorption in metal-halide perovskite solar cells, Solar RRL **5**, 2100029 (2021).
[85] J. Shin, G. A. Gamage, Z. Ding, K. Chen, F. Tian, X. Qian, J. Zhou, H. Lee, J. Zhou, L. Shi, *et al.*, High ambipolar mobility in cubic boron arsenide, Science **377**, 437 (2022).
[86] J. Li, Z.-K. Yuan, S. Chen, X.-G. Gong, and S.-H. Wei, Effective and noneffective recombination center defects in $Cu_2ZnSnS_4$: Significant difference in carrier capture cross sections, Chem. Mater. **31**, 826 (2019).
[87] B. Das, I. Aguilera, U. Rau, and T. Kirchartz, What is a deep defect? combining Shockley-Read-Hall statistics with multiphonon recombination theory, Phys. Rev. Mater. **4**, 024602 (2020).
[88] Y. Wang, N. Sato, K. Yamada, and T. Fujino, Synthesis of $BaZrS_3$ in the presence of excess sulfur, J. Alloys. Compd. **311**, 214 (2000).
[89] C. Comparotto, P. Strom, O. Donzel-Gargand, T. Kubart, and J. J. Scragg, Synthesis of $BaZrS_3$ perovskite thin films at a moderate temperature on conductive substrates, ACS Appl. Energy Mater. **5**, 6335 (2022).
[90] B. Zhao, H. Chen, R. Ahsan, F. Hou, E. R. Hoglund, S. Singh, M. Shanmugasundaram, H. Zhao, A. V. Krayev, H. Htoon, *et al.*, Photoconductive effects in single crystals of $BaZrS_3$, ACS Photonics **11**, 1109 (2024).
[91] A. Baumann, S. Väth, P. Rieder, M. C. Heiber, K. Tvingstedt, and V. Dyakonov, Identification of trap states in perovskite solar cells, J. Phys. Chem. Lett. **6**, 2350 (2015).
[92] S. Heo, G. Seo, Y. Lee, D. Lee, M. Seol, J. Lee, J.-B. Park, K. Kim, D.-J. Yun, Y. S. Kim, *et al.*, Deep level trapped defect analysis in $CH_3NH_3PbI_3$ perovskite solar cells by deep level transient spectroscopy, Energy Environ. Sci. **10**, 1128 (2017).
[93] W. S. Yang, B.-W. Park, E. H. Jung, N. J. Jeon, Y. C. Kim, D. U. Lee, S. S. Shin, J. Seo, E. K. Kim, J. H. Noh, *et al.*, Iodide management in formamidinium-lead-halide–based perovskite layers for efficient solar cells, Science **356**, 1376 (2017).
[94] G. Hodes and P. V. Kamat, Understanding the implication of carrier diffusion length in photovoltaic cells, J. Phys. Chem. Lett. **6**, 4090 (2015).
[95] A. Crovetto, A figure-of-merit-based framework to evaluate photovoltaic materials, arXiv:2404.14732.
[96] L. D. Whalley, J. M. Frost, Y.-K. Jung, and A. Walsh, Perspective: Theory and simulation of hybrid halide perovskites, J. Chem. Phys. **146**, 220901 (2017).
[97] J. Pandey, D. Ghoshal, D. Dey, T. Gupta, A. Taraphder, N. Koratkar, and A. Soni, Local ferroelectric polarization in antiferroelectric chalcogenide perovskite $BaZrS_3$ thin films, Phys. Rev. B **102**, 205308 (2020).
[98] A. M. Ganose, J. Park, A. Faghaninia, R. Woods-Robinson, K. A. Persson, and A. Jain, Efficient calculation of carrier scattering rates from first principles, Nat. Commun. **12**, 2222 (2021).
[99] G. Kresse and J. Furthmüller, Efficient iterative schemes for ab initio total-energy calculations using a plane-wave basis set, Phys. Rev. B **54**, 11169 (1996).
[100] G. Kresse and D. Joubert, From ultrasoft pseudopotentials to the projector augmented-wave method, Phys. Rev. B **59**, 1758 (1999).

[101] J. P. Perdew, A. Ruzsinszky, G. I. Csonka, O. A. Vydrov, G. E. Scuseria, L. A. Constantin, X. Zhou, and K. Burke, Restoring the density-gradient expansion for exchange in solids and surfaces, Phys. Rev. Lett. **100**, 136406 (2008).

[102] S. Baroni, P. Giannozzi, and A. Testa, Elastic constants of crystals from linear-response theory, Phys. Rev. Lett. **59**, 2662 (1987).

[103] F. Giustino, Electron-phonon interactions from first principles, Rev. Mod. Phys. **89**, 015003 (2017).

[104] R. Lelieveld and D. Ijdo, Sulphides with the $GdFeO_3$ structure, Acta Crystallogr. B: Struct. Crystallogr. Cryst. Chem. **36**, 2223 (1980).

[105] S. Zhang, S.-H. Wei, A. Zunger, and H. Katayama-Yoshida, Defect physics of the $CuInSe_2$ chalcopyrite semiconductor, Phys. Rev. B **57**, 9642 (1998).

[106] C. Freysoldt, B. Grabowski, T. Hickel, J. Neugebauer, G. Kresse, A. Janotti, and C. G. Van de Walle, First-principles calculations for point defects in solids, Rev. Mod. Phys. **86**, 253 (2014).

[107] C. Freysoldt, J. Neugebauer, and C. G. Van de Walle, Fully ab initio finite-size corrections for charged-defect supercell calculations, Phys. Rev. Lett. **102**, 016402 (2009).

[108] Y. Kumagai and F. Oba, Electrostatics-based finite-size corrections for first-principles point defect calculations, Phys. Rev. B **89**, 195205 (2014).

[109] J. P. Perdew, K. Burke, and M. Ernzerhof, Generalized gradient approximation made simple, Phys. Rev. Lett. **77**, 3865 (1996).

[110] D. Broberg, B. Medasani, N. E. Zimmermann, G. Yu, A. Canning, M. Haranczyk, M. Asta, and G. Hautier, PyCDT: A python toolkit for modeling point defects in semiconductors and insulators, Comput. Phys. Commun. **226**, 165 (2018).

[111] C. G. Van de Walle and J. Neugebauer, First-principles calculations for defects and impurities: Applications to III-nitrides, J. Appl. Phys. **95**, 3851 (2004).

[112] J. Ma, S.-H. Wei, T. Gessert, and K. K. Chin, Carrier density and compensation in semiconductors with multiple dopants and multiple transition energy levels: Case of Cu impurities in CdTe, Phys. Rev. B **83**, 245207 (2011).

[113] Y. Kumagai, M. Choi, Y. Nose, and F. Oba, First-principles study of point defects in chalcopyrite $ZnSnP_2$, Phys. Rev. B **90**, 125202 (2014).

[114] J.-H. Yang, J.-S. Park, J. Kang, W. Metzger, T. Barnes, and S.-H. Wei, Tuning the Fermi level beyond the equilibrium doping limit through quenching: The case of CdTe, Phys. Rev. B **90**, 245202 (2014).

[115] S. P. Ong, W. D. Richards, A. Jain, G. Hautier, M. Kocher, S. Cholia, D. Gunter, V. L. Chevrier, K. A. Persson, and G. Ceder, Python Materials Genomics (pymatgen): A robust, open-source Python library for materials analysis, Comput. Mater. Sci. **68**, 314 (2013).

[116] Y. Kumagai, N. Tsunoda, A. Takahashi, and F. Oba, Insights into oxygen vacancies from high-throughput first-principles calculations, Phys. Rev. Mater. **5**, 123803 (2021).

[117] A. G. Squires, D. O. Scanlon, and B. J. Morgan, py-sc-fermi: Self-consistent Fermi energies and defect concentrations from electronic structure calculations, J. Open Source Softw. **8**, 4962 (2023).

[118] K. Momma and F. Izumi, VESTA 3 for three-dimensional visualization of crystal, volumetric and morphology data, J. Appl. Crystallogr. **44**, 1272 (2011).

[119] A. M. Ganose, A. J. Jackson, and D. O. Scanlon, sumo: Command-line tools for plotting and analysis of periodic ab initio calculations, J. Open Source Softw. **3**, 717 (2018).

[120] A. M. Stoneham, *Theory of Defects in Solids: Electronic Structure of Defects in Insulators and Semiconductors* (Oxford University Press, Oxford, UK, 2001).

[121] C. Henry and D. V. Lang, Nonradiative capture and recombination by multiphonon emission in GaAs and GaP, Phys. Rev. B **15**, 989 (1977).

[122] S. Kim, S. N. Hood, and A. Walsh, Anharmonic lattice relaxation during nonradiative carrier capture, Phys. Rev. B **100**, 041202 (2019).

[123] L. Shi, K. Xu, and L.-W. Wang, Comparative study of ab initio nonradiative recombination rate calculations under different formalisms, Phys. Rev. B **91**, 205315 (2015).

[124] M. E. Turiansky, A. Alkauskas, M. Engel, G. Kresse, D. Wickramaratne, J.-X. Shen, C. E. Dreyer, and C. G. Van de Walle, Nonrad: Computing nonradiative capture coefficients from first principles, Comput. Phys. Commun. **267**, 108056 (2021).

[125] S. Kim, S. N. Hood, P. van Gerwen, L. D. Whalley, and A. Walsh, CarrierCapture.jl: Anharmonic carrier capture, J. Open Source Softw. **5**, 2102 (2020).

[126] https://doi.org/10.17172/nomad/2024.08.08-1.

[127] F. Ricci, W. Chen, U. Aydemir, G. J. Snyder, G.-M. Rignanese, A. Jain, and G. Hautier, An ab initio electronic transport database for inorganic materials, Sci. Data **4**, 1 (2017).

[128] R. Claes, G. Brunin, M. Giantomassi, G.-M. Rignanese, and G. Hautier, Assessing the quality of relaxation-time approximations with fully automated computations of phonon-limited mobilities, Phys. Rev. B **106**, 094302 (2022).

[129] J. Willis, R. Claes, Q. Zhou, M. Giantomassi, G.-M. Rignanese, G. Hautier, and D. O. Scanlon, Limits to hole mobility and doping in copper iodide, Chem. Mater. **35**, 8995–9006 (2023).

[130] J. M. Skelton, D. S. D. Gunn, S. Metz, and S. C. Parker, Accuracy of hybrid functionals with non-self-consistent kohn-sham orbitals for predicting the properties of semiconductors, J. Chem. Theory Comput. **16**, 3543 (2020).

[131] S. Filippone, B. Zhao, S. Niu, N. Z. Koocher, D. Silevitch, I. Fina, J. M. Rondinelli, J. Ravichandran, and R. Jaramillo, Discovery of highly polarizable semiconductors $BaZrS_3$ and $Ba_3Zr_2S_7$, Phys. Rev. Mater. **4**, 091601 (2020).

[132] P. Kayastha, D. Tiwari, A. Holland, O. S. Hutter, K. Durose, L. D. Whalley, and G. Longo, High-temperature equilibrium of 3d and 2d chalcogenide perovskites, Sol. RRL **7**, 2201078 (2023).

[133] A. Jain, S. P. Ong, G. Hautier, W. Chen, W. D. Richards, S. Dacek, S. Cholia, D. Gunter, D. Skinner, G. Ceder, *et al.*, Commentary: The materials project: A materials genome approach to accelerating materials innovation, APL Mater. **1**, 011002 (2013).